Carbohydrate Polymers 389 (2026) 125616



Contents lists available at ScienceDirect

Carbohydrate Polymers

journal homepage: www.elsevier.com/locate/carbpol



Exploring the Hofmeister effect on guar gum dispersions: a machine learning and data fusion approach combining infrared spectroscopy and thermal analysis

Duccio Tatini [a,b,*], Mert Acar [b,c], Michele Baglioni [a,b], Gabriella Tamasi [a,b], Claudio Rossi [a,b], Pierandrea Lo Nostro [b,c]

[a] Department of Biotechnology Chemistry and Pharmacy, University of Siena, 53100, Siena, Italy
[b] Centre for Colloid and Surface Science (CSGI), University of Florence, Via della Lastruccia 3, 50019, Sesto Fiorentino, Italy
[c] Department of Chemistry "Ugo Schiff", University of Florence, 50019 Sesto Fiorentino, Firenze, Italy

ARTICLE INFO

Keywords:
Specific ion effect
Soft matter
Guar gum
Macromolecules
Chemometrics
Multi-block analysis

ABSTRACT

Specific ion effects, as described by the Hofmeister series, play a crucial role in modulating the physicochemical behavior of macromolecular systems. In polysaccharide aqueous dispersions these effects are closely related to modifications of the polymer–water hydrogen-bonding network, although their interpretation remains challenging due to the complex interplay between ions, water, and macromolecular structure. In this study, we investigate the effect of kosmotropic and chaotropic cosolutes on guar gum aqueous dispersions by integrating Attenuated Total Reflectance–Fourier Transform Infrared (ATR-FTIR) spectroscopy and thermogravimetric analysis (TGA) using multivariate analysis and data fusion strategies. Distinct ion-specific modifications were observed in both the hydroxyl stretching region and the dehydration behavior of the galactomannan system. Principal Component Analysis (PCA) applied to the individual datasets revealed distinct ion-specific trends while a mid-level data fusion approach based on the Common Dimensions (ComDim) algorithm further improved sample clustering and visualization. Loading and salience analyses identified the main spectral and thermal features associated with ion-dependent perturbations of the guar gum–water network. The proposed methodology highlights the potential of integrated spectroscopic, thermal, and chemometric approaches for investigating hydration-mediated phenomena in polysaccharide systems and, more broadly, in complex macromolecular materials.

1. Introduction

Specific ion effects, often described in terms of Hofmeister series, refer to the modifications induced by the presence of electrolytes on the physical and chemical behavior of systems belonging to the macromolecular and colloidal realms (Gregory et al., 2022; Lo Nostro & Ninham, 2012; Salis & Ninham, 2014). First observed in the context of protein precipitation, the Hofmeister series ranks ions according to their ability to stabilize or destabilize macromolecules in aqueous solution (Cacace et al., 1997; Kunz et al., 2004). These effects are now acknowledged across a wide range of systems, including proteins, polysaccharides, surfactants, membranes, hydrogels, in water and in non-aqueous solvents, where they modify parameters and affect phenomena such as solubility, aggregation, conformational stability, and hydration just to mention a few (Acar, Tatini, Fidi, et al., 2024; Boström et al., 2003; Lin et al., 2020; Musilová et al., 2019; Sarri et al., 2018; Tatini et al., 2017; Tatini et al., 2022). Beyond their fundamental relevance from a physicochemical perspective, Hofmeister phenomena also have important implications for the formulation, stability, and functional performance of macromolecular systems in technological and industrial applications. Although the underlying mechanisms are multifaceted—encompassing ion hydration, dispersion forces, interfacial adsorption, and water structure modulation—they remain only partly understood, due to their complexity and to their mutual interconnection (Acar et al., 2025; Ninham & Yaminsky, 1997; Parsons et al., 2011). Experimental studies on Hofmeister effects traditionally rely on monitoring the changes in physicochemical properties (e.g., solubility, spectral features, thermal transitions, mechanical and rheological properties) across a series of

* Corresponding author at: Department of Biotechnology Chemistry and Pharmacy, University of Siena, 53100, Siena, Italy.
E-mail address: duccio.tatini@unisi.it (D. Tatini).

https://doi.org/10.1016/j.carbpol.2026.125616
Received 21 January 2026; Received in revised form 30 June 2026; Accepted 2 July 2026
Available online 3 July 2026
0144-8617/© 2026 The Authors. Published by Elsevier Ltd. This is an open access article under the CC BY-NC-ND license (http://creativecommons.org/licenses/by-nc-nd/4.0/).

salts, and interpreting these changes by correlating them with known ion-specific descriptors (e.g., ionic static polarizability, Gibbs free energy and entropy of hydration, Jones-Dole viscosity coefficient, lyotropic number etc.) (Jenkins & Marcus, 1995; Marcus, 1991; Tatini et al., 2022; Voet, 1937). This approach often involves visual trend recognition, requiring manual data processing and interpretation, which may be time and labor-consuming.

In recent years, machine learning and chemometrics have gained increasing attraction in analytical chemistry as powerful tools for pattern recognition, data exploration, and classification in high-dimensional experimental datasets (Houhou & Bocklitz, 2021; H.-P. Wang et al., 2022). Among these, Principal Component Analysis (PCA) stands out as a widely used unsupervised method that reduces data dimensionality while preserving variance (Bro & Smilde, 2014; Cordella, 2012). PCA allows for the visualization of sample distribution in lower-dimensional space (typically 2D or 3D), making it particularly useful for detecting trends and grouping behavior without requiring an a priori information (Greenacre et al., 2022). By analyzing principal component loadings, researchers can identify which variables—depending on the experimental techniques used to generate the dataset—provide the predominant contributions to sample differentiation. PCA thus offers an objective and data-driven alternative to traditional descriptive analyses. Key applications of PCA in analytical chemistry include classification of complex mixtures, process monitoring, metabolomic profiling, and food authentication (Borghini et al., 2024; Jiang et al., 2013; Kemsley et al., 2019; McKenzie et al., 2011; Nardin et al., 2024; Salvatore et al., 2013; Tamasi et al., 2019).

To further enhance interpretation and classification when multiple types of measurements are involved, data fusion strategies can be successfully implemented (Biancolillo et al., 2019; Mishra et al., 2021). Data fusion refers to the integration of data from different sources or analytical techniques to exploit complementary information and uncover relationships that may not be apparent from single-block (or single-technique) analysis (Azcarate et al., 2021). Data fusion can be implemented at different levels: low-level (combining raw data), mid-level (merging extracted features), or high-level (integrating final results) (Borràs et al., 2015). Among mid-level approaches, the Common Dimensions (ComDim) algorithm has emerged as a robust unsupervised method for multiblock analysis (Rocha Baqueta et al., 2021; Tatini et al., 2025; Tomassetti et al., 2024; Tomassetti, Marini, Di Natale, et al., 2025; Tomassetti, Marini, Pezzilli, et al., 2025). ComDim identifies shared latent structures across multiple datasets while also quantifying the contribution (salience) of each block to those structures, enabling an integrated data visualization and more effective sample discrimination (Cariou et al., 2018; Tchandao Mangamana et al., 2019).

This work investigates the influence of kosmotropic and chaotropic cosolutes on the hydration and physicochemical behavior of guar gum aqueous dispersions by combining ATR-FTIR spectroscopy and thermogravimetric analysis (TGA) with an original multivariate data fusion approach. PCA and ComDim are employed as exploratory tools to resolve ion-specific trends within the spectroscopic and thermal datasets and to identify the relevant features associated with different hydration environments and dehydration processes that drive the differentiation according to the Hofmeister series.

Guar gum is a neutral galactomannan consisting of a linear mannan backbone (β-(1,4)-linked) with the galactose units attached as single side chains by an α-(1,6)-glycosidic linkage. Among naturally occurring galactomannans, guar gum is one of the most extensively produced and commercially used polysaccharides worldwide, owing to its remarkable thickening, viscosifying, and stabilizing properties (García et al., 2025; Özen et al., 2023). In aqueous systems the physicochemical behavior of guar gum strongly depends on polymer concentration, as typically observed for flexible water-soluble polysaccharides. At very low concentrations the polymer chains are isolated and do not significantly interact. Upon increasing concentration the system enters the semi-dilute regime, where chain overlap occurs and intermolecular interactions become relevant, leading to the formation of a transient, highly hydrated network. At even higher concentrations the strong entanglement effects and increased viscosity dominate the macroscopic behavior (Torres et al., 2014; Q. Wang et al., 2003). Under these conditions, the solvent molecules become increasingly constrained by the polymer network itself, potentially reducing the relative contribution of ion-specific phenomena to the overall physicochemical response. At the concentration used in this study (1% *w*/w) guar gum dispersions fall within the semi-dilute regime. In this condition, the high density of hydroxyl groups along both the mannan backbone and the galactose side chains promotes extensive hydrogen bonding with water, resulting in a heterogeneous hydration environment comprising bulk-like water, polymer-associated water, and more strongly bound hydration layers.

Within this framework the presence of kosmotropic and chaotropic cosolutes alters the polymer–water network, and ion-specific interactions can perturb the distribution and strength of hydrogen-bonded water populations. This makes guar gum dispersions a well-suited system for probing Hofmeister-driven phenomena in terms of their impact on polysaccharide hydration and associated physicochemical properties. In galactomannans these hydration-mediated interactions are directly connected to functional properties such as viscosity, chain association, rheological behavior and thermal stability. Understanding how different cosolutes perturb the guar gum–water network is therefore relevant not only from a fundamental physicochemical perspective, but also for the rational tuning of polysaccharide-based formulations.

Moreover, the broad technological relevance of GG in food, pharmaceutical, and oilfield formulations underscores the importance of understanding how electrolytes and cosolutes modulate its hydration and stability under application-relevant conditions. (George et al., 2019; Sarri et al., 2019; Sharahi et al., 2025; Sharma et al., 2018). In this study, we examined a representative series of anions spanning the Hofmeister series, namely Na_2SO_4, NaF, NaCl, NaBr, NaI, and NaSCN, together with two non-ionic modifiers, trehalose and urea. These latter cosolutes were included because they exhibit a pronounced kosmotropic and chaotropic character respectively while maintaining electrical neutrality, thereby allowing the isolation of water-structuring effects from purely ionic contributions.

We test the hypothesis that specific ion effects related to modifications in the hydration and physicochemical behavior of guar gum can be effectively identified by multivariate analysis and data fusion. This rapid and data-driven approach provides insights into the role of ionic and molecular modifiers in modulating the functional properties of guar gum formulations, with direct implications for technological contexts ranging from texture engineering in foods and drug delivery systems to viscosity control in hydraulic fracturing fluids and personal care products.

To the best of our knowledge, only one previous study has applied chemometric tools to explore kosmotropic and chaotropic ion properties in relation to the Hofmeister series (Jakubowska & Kozik, 2019), while no previous work has combined ATR-FTIR, thermogravimetric analysis, and multi-technique data fusion to investigate specific ion effects in guar gum dispersions. The present study therefore aims to provide a physicochemical interpretation on how different cosolutes modulate hydration and thermal behavior in a galactomannan system, also highlighting the potential of integrated spectroscopic and thermal approaches for the investigation of ion–polysaccharide interactions.

2. Materials and methods

2.1. Materials

All chemicals were reagent grade (≥99%) and used without further purifications. NaF, NaI, NaSCN, were purchased from Fluka (Milan, Italy). NaCl, NaBr, Na_2SO_4 and trehalose were supplied by Sigma-Aldrich (Milan, Italy). Urea was purchased from Riedel de Haen (Germany) and guar gum was supplied by Lamberti S.p.A. (GUAR GUM 3500

/ 5000, purity >90%, $M_w = 2 \times 10^6$ Da, mannose-to-galactose (M/G) ratio 1.8–2.0:1, Albizzate, Italy). The molecular weight provided by the supplier was confirmed by dilute-solution viscometry measurements. Five guar gum solutions were prepared with concentrations ranging from 0.01 to 0.06% (*w/v*) using water as solvent. Flow times were measured at 25 °C using an Ubbelohde capillary viscometer (Schott, Germany). The intrinsic viscosity [η] was obtained by extrapolation to zero concentration through linear regression of the reduced viscosity versus concentration plot (Fig. S1 in the Supplementary Material). The intrinsic viscosity was subsequently used to estimate the molecular weight of the guar gum sample by means of the Mark–Houwink–Sakurada relationship:

$$[\eta] = K \cdot M^{\alpha} \quad (1)$$

where M is the molecular weight estimated from intrinsic viscosity, $K = 3.8 \cdot 10^{-2}$ mL/g and $\alpha = 0.723$, according to literature values reported for unmodified guar gum in aqueous solution (Cheng et al., 2002; Robinson et al., 1982).

All solutions and dispersions were prepared with bidistilled Milli-Q water (resistivity>18 MΩ·cm at 25 °C).

2.2. Sample preparation

The dispersions were prepared by slowly adding a weighted amount of guar gum powder to water or 0.5 M salt solutions under constant stirring at room temperature (21 ± 1 °C). The final concentration of GG was 1% *w*/w for all the samples.

To assess the possible influence of residual impurities, control experiments were performed on guar gum samples after purification. A 1% w/w guar gum dispersion was prepared in Milli-Q water and stirred overnight at 25 °C to ensure complete hydration of the polysaccharide. The resulting dispersion was filtered through cloth to remove insoluble residues and particulate material. The polymer was subsequently recovered by precipitation using two volumes of ethanol. The precipitated guar gum was collected, dried, and subsequently redispersed in water or selected salt solutions (1% *w*/w) for the analyses.

2.3. Attenuated total reflection Fourier-transform infrared spectroscopy (ATR-FTIR)

The ATR-FTIR spectra were acquired on a Thermo Nicolet Nexus 870 FT-IR spectrophotometer equipped with a liquid nitrogen cooled MCT (mercury-cadmium-telluride) detector. The spectra were collected within the 4000–1000 cm^{-1} range using a spectral resolution of 2 cm^{-1} and 128 scans per run. Each spectrum was corrected to remove the contribution of the atmospheric CO_2 and subtract the background. The effect of the different anions on the spectral features of the GG samples was investigated by deconvoluting the -OH stretching band in the 3700 and 3000 cm^{-1} region using Gaussian curves and a constant baseline. Prior to chemometrics analysis, several preprocessing techniques were tested: the most suitable approach was a first derivative using a Savitzsky-Golay filter (13 points window and third order for the interpolating polynomial) in combination with a data normalization by the norm.

2.4. Thermogravimetric analysis (TGA)

Thermogravimetric analyses were performed with a SDT Q600 apparatus (TA Instruments, New Castle, USA). A weighted amount of sample was placed in an open aluminum pan and measured against an empty reference while heating from 25 °C to 450 °C, with a heating rate of 10 °C/min and a constant N_2 flow rate of 100 mL/min. The first derivative of the weight loss as a function of temperature followed by a normalization by the norm was used as input for the chemometrics analysis.

2.5. Differential scanning calorimetry (DSC)

DSC characterization of guar gum powder was performed on a DSC-Q2000 by TA Instruments (Philadelphia, PA). The sample was equilibrated at −10 °C, then heated up to 110 °C with a ramp of 5 °C/min. Experiments were performed in N_2 atmosphere, with a flow rate of 50 mL/min.

2.6. Chemometric methods

An exploratory Principal Component Analysis (PCA) was performed on the individual datasets from ATR-FTIR and TGA experiments in order to analyze common features and detect potential clustering among the samples. PCA is a dimensionality reduction technique: the data compression is performed by projecting the samples onto a low dimensional subspace, in which the axes, known as principal components (PCs), are oriented in the directions where the variance in the data is maximum (Li Vigni et al., 2013). The mathematical computation involves the calculation of the covariance matrix of the input dataset to capture the relationships between variables. Eigenvalues and eigenvectors of the covariance matrix are determined, with eigenvectors corresponding to the principal components and eigenvalues indicating the variance explained by each component. The analysis of the loadings, i.e. the correlation coefficients between the original variables and the principal components, highlights the contribution of each original variable to the different components. The scores, which represent the projections of the data onto the principal components, were used to visualize clustering or patterns within the dataset. Further details about this method can be found in the reviews of Greenacre, Cadima and Beattie (Beattie & Esmonde-White, 2021; Greenacre et al., 2022; Jolliffe & Cadima, 2016).

Common Dimensions (ComDim) analysis is a mid-level data fusion technique that identifies shared patterns across multiple datasets (or blocks) of variables, while also retaining individual block-specific features. ComDim is an implementation of the Common Components and Specific Weights Analysis (CCSWA) procedure developed by Qannari and can be viewed as a multiblock weighted principal components analysis (Qannari et al., 1995; Rosa et al., 2017). The datasets from ATR-FTIR and thermogravimetric analysis were concatenated, and each block was normalized using its Frobenius norm to ensure that all blocks contribute equally in terms of total variance (Zeaiter & Rutledge, 2009).

The ComDim algorithm operates on the variance-covariance matrices of the samples, which share identical dimensions. This enables the computation of a weighted sum of these matrices, from which the first normalized principal component, usually referred as “Common Dimension” (CD), is derived. Iteratively, the algorithm refines the weight or “salience” associated with each data block to optimize the identified CD. The salience indicates the contribution of the different variables within each block to the common dimensions. Once the first CD is established, each data block matrix is deflated, and the procedure is repeated to extract additional CDs. Consequently, each CD corresponds to the leading principal component of the weighted variance-covariance matrix sum of the deflated blocks (Jouan-Rimbaud Bouveresse et al., 2011; Rosa et al., 2017). The common components were ranked based on their contribution to shared variance across blocks, while block-specific components captured individual dataset characteristics. For visualization purposes in the ComDim analysis the data are projected onto the common dimensions' subspace (score plot) to evaluate clustering, patterns, or relationships across datasets. The saliences and loadings (i.e. the individual contribution of the original variables to each CD) plots show the sources of the variables responsible for the similarities and differences among the samples (You et al., 2023). All computations were carried out using the MBA-GUI toolbox for MATLAB (Mishra et al., 2020).

3. Results and discussion

The physicochemical properties of the guar gum powder used in this study were preliminarily assessed by ATR-FTIR spectroscopy, differential scanning calorimetry and thermogravimetric analysis. In addition, the molecular weight estimated from the intrinsic viscosity of guar gum dilute solutions in water as solvent using the Mark–Houwink–Sakurada relationship was found to be in good agreement with the value reported by the supplier (Fig. S1 and Table S1 in the Supplementary Material). The ATR-FTIR spectrum exhibits the characteristic features of guar gum and galactomannan polysaccharides, including the broad OH stretching band around 3300 cm^{-1}, CH stretching vibrations near 2900 cm^{-1}, and the carbohydrate fingerprint region between 1200 and 800 cm^{-1} (Anjum et al., 2021). DSC analysis shows a glass transition with an associated enthalpic relaxation centered around 60 °C, while TGA reveals the typical thermal behavior of guar gum, consisting of an initial weight loss attributed to residual moisture followed by a single major decomposition event centered at approximately 300 °C (Vulpitta et al., 2025). The IR spectrum and the thermograms for the GG powder are reported in Fig. S2 in the Supplementary Material.

In the following sections, the results obtained from the ATR-FTIR and TGA experiments for the guar-based polysaccharide dispersions will be discussed separately. Then, the outcomes of the multiblock analysis on the merged datasets based on the ComDim approach will be presented.

3.1. ATR-FTIR

The ATR-FTIR spectra for the GG dispersions in the presence of the different anions are reported in Fig. 1.

All samples show the characteristic spectral signature of guar gum water dispersions (Rébufa et al., 2019). The broad band between 3700 and 3000 cm^{-1} is attributed to the O—H stretching vibrations occurring in water molecules and hydroxyl groups in the polysaccharide chains, while in the region 3000–2800 cm^{-1} the two small peaks located at approximately 2920 and 2850 cm^{-1} are assigned to the antisymmetric and symmetric C—H stretching vibrations in methylene groups respectively. The intense signal located at 1640 cm^{-1} is ascribed to the O—H bending, however a small contribution to this band can derive from the axial deformation of the C═O bond (amide band I) due to the presence of proteins and amino acids impurities from guar seed and coat. Additional signals with lower intensities can be detected around 1740 cm^{-1} (C═O stretching vibration from esters and amides) and 1540 cm^{-1} (NH_2 deformation), confirming the presence of amino acids impurities which are not removed during the guar seed purification processes (Abidi et al., 2014; Liyanage et al., 2015). Other minor impurities like ash, crude fiber and husk residues may also be present in commercial guar gum (Cunha et al., 2007). It should be noted, however, that all the investigated samples were prepared using the same guar gum batch. Therefore, the compositional heterogeneity associated with these residual components remained constant throughout the experimental set. While these components may generate minor spectral features, as in the 1500–1800 cm^{-1} range, and contribute as an identical background across the samples, they are not expected to influence the systematic kosmotropic/chaotropic trends. This interpretation is further supported by additional control experiments performed on purified guar gum obtained by dissolution in water, filtration, and ethanol precipitation (Sharahi et al., 2025). Purified samples including 1% *w*/w GG in water and selected kosmotropic and chaotropic cosolutes were analyzed by ATR-FTIR and TGA, revealing no significant differences compared to the pristine systems within the experimental sensitivity of the techniques. The comparison between purified and non-purified guar gum dispersions in water at 1% is reported in Fig. S3 in the Supplementary Material as an illustrative example. The spectral region comprised between 1300 and 1000 cm^{-1} shows multiple bands that can be assigned to the vibrations of the glycosidic bonds within the galactomannan backbone (Mudgil et al., 2012).

The effect of the polysaccharide and of the different cosolutes on the spectral features emerges clearly. In fact, the addition of GG and of the background electrolytes results in a variation of the O—H stretching band intensity at 3700–3000 cm^{-1}, along with a shift of the peak maximum towards higher wavenumbers. Moreover, the presence of the different cosolutes seems to affect also the band shape, suggesting a modification in the relative contributions of the different subpopulations of O—H groups in this region. In general, a decrease in the O—H stretching bandwidth and intensity, together with a shift to higher wavenumbers indicate a decrease in hydrogen bond (HB) strength, number or linearity in the system (Enev et al., 2019; Grossutti & Dutcher, 2016). When compared to pure water (i.e. without GG and salts) the O—H stretching band intensity increases in the presence of GG and kosmotropic species, while it shows a decrease upon the addition of chaotropic species. Interestingly, the highest absorbance value is observed for the 1% GG dispersion with no added cosolutes. This behavior can be attributed to the strong hydration of the polysaccharide chains, which promotes the formation of an extended hydrogen-bonding network involving both water molecules and the hydroxyl groups of guar gum. The resulting increase in the number and heterogeneity of hydrogen bonds leads to a higher infrared absorption intensity in the O—H stretching region. In this condition, the structuring effect of the polysaccharide dominates the spectral response, and no additional cooperative strengthening of the hydrogen-bond network is observed

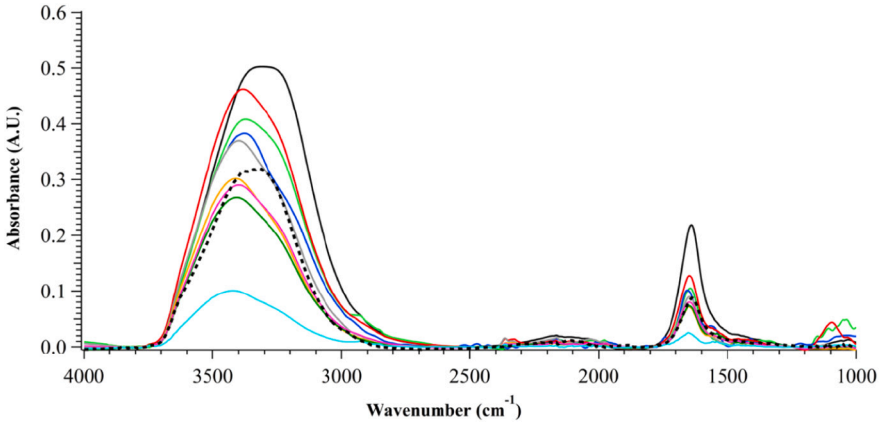


Fig. 1. Attenuated Total Reflection-Fourier Transform Infrared (ATR-FTIR) spectra between 4000 and 1000 cm^{-1} for GG 1% dispersion (black) and GG in the presence of 0.5 M Na_2SO_4 (red), trehalose (light green), NaF (blue), NaCl (grey), NaBr (orange), NaI (dark green), NaSCN (light blue) and urea (pink). The dotted line represents the ATR-FTIR spectrum of pure water. (For interpretation of the references to colour in this figure legend, the reader is referred to the web version of this article.)

upon the addition of kosmotropic species SO_4^{2-}, F^- and trehalose. Due to their high charge density and small polarizability, they compete with the hydroxyl groups of the polysaccharide for water molecules, leading to a redistribution of hydration water populations between solvated ions and polymer-associated domains. Consequently, although the presence of kosmotropic species brings about an increase in the OH stretching intensities if compared to pure water, the corresponding IR absorption remains lower than that of the pristine guar gum dispersion, where the polymer hydration network is highly structured.

In the case of chaotropic anions (Br^-, I^-, SCN^-) and urea the nature of the cosolute overcomes the strengthening effect of GG, resulting in an overall decrease in the band intensity. The intensity trend can be summarized as follows:

for the ionic species: no salt 1% GG > SO_4^{2-} > F^- > Cl^- > pure water > Br^- > I^- > SCN^-

for the non-ionic species: no salt 1% GG > trehalose > pure water > urea.

The bandwidth value (indicated as the Full Width at Half Maximum, FWHM), the position of the peak maximum and the Center of Gravity (CoG) for the O—H stretching band are listed in Table 1. For better comparison these descriptors are plotted as a function of the different salts and cosolutes in Fig. S4 and S5 in the Supplementary Material. If compared to pure water all the samples show higher FWHM values, evidencing the structuring effect of GG on the hydrogen bond network. The presence of kosmotropic species does not remarkably affect the bandwidth observed for the aqueous 1% GG dispersion, while the addition of chaotropic species brings about a significant decrease in the FWHM value, confirming their structure-breaking nature.

The peak maximum and the CoG values show a similar trend: in the GG water dispersion they are both red-shifted, but moving from kosmotropic to chaotropic species their position progressively shifts towards higher values. These results confirm the presence of two simultaneous contributions, i.e. (i) the structuring effect of the polysaccharide and (ii) the structure enhancing/breaking effect of the anions or cosolutes according to the Hofmeister series. The behavior of kosmotropic species is counterintuitive, since they do not play a synergistic role in strengthening the hydrogen bonding network. This effect can be explained by considering the hydration process of the polysaccharide macromolecules: water interacts with the hydroxyl groups of guar gum, forming a dynamic three-dimensional hydrogen bonded network where HB continuously break and reform. In this process, kosmotropic ions, owing to their strong hydration and high charge density, preferentially interact with bulk water, thereby competing with guar gum hydroxyl groups for hydrogen-bonded water molecules. This competition perturbs the hydration shell of the polysaccharide without direct ion adsorption, resulting in a redistribution of hydrogen-bond populations rather than a cooperative strengthening of the network. Consistently, the ATR-FTIR spectra show no further increase in the O—H stretching band intensity with respect to the pristine GG/water dispersion, while only modest variations in FWHM, center of gravity, and peak position are observed. In contrast, chaotropic ions are more weakly hydrated and more polarizable, which favors their partial adsorption at the polymer–water interface. This interaction disrupts local hydrogen-bond cooperativity, promotes partial chain expansion, and reduces the structuring of hydration water, leading to a decrease in O—H stretching intensity and a shift towards higher wavenumbers, consistent with an overall structure-breaking effect. This proposed mechanism is in good agreement with the results reported in a previous study from our research group on the influence of different anions and solutes on the thermal and rheological properties of GG dispersions (Tatini et al., 2017).

To further elucidate the effect of the different salts and cosolutes on the interaction between guar gum chains and water in the dispersed systems, the O—H stretching band was deconvoluted into three contributions, according to the literature (Enev et al., 2019; Liu et al., 2004). Peak 1, located between 3574 and 3591 cm^{-1}, is attributed to the coupling of the O—H asymmetric stretching modes in water molecules within a disordered HB network, and it is usually referred to as liquid-like or multimer water (Acar et al., 2025; Binder, 2007; Enev et al., 2019; Grossutti & Dutcher, 2016). Peak 2 (3427–3467 cm^{-1}) can be associated with intermediate or distorted hydrogen-bonding environments, often attributed in the literature to less ordered water clusters such as distorted tetrameric or pentameric arrangements (Barbar et al., 2023; Grossutti & Dutcher, 2020; Madeira et al., 2021; Marinov et al., 2001). The low-frequency contribution located between 3260 and 3313 cm^{-1} (peak 3) is related to tetrahedrally coordinated water molecules, i.e. water pentamers, which are involved in strong intermolecular and symmetrical hydrogen bonds (Kitadai et al., 2014; Liu et al., 2004).

Fig. S6 in the Supplementary Material shows all deconvoluted spectra and their corresponding assignments. In Table 1 the relative areas for the three different contributions, the maximum peak positions and the peak shift $\Delta\underline{\nu}$, defined as the difference between the maximum peak wavenumber in the presence of salt and the peak maximum in the pure water system, are listed. For better comparison the relative areas, the peak maxima and the peak shifts for the different salts are plotted in Figs. S7, S8 and S9 respectively in the Supplementary Material.

From the analysis of the relative areas, the contribution provided by water molecules involved in a disordered HB network (peak 1) shows a small increase upon the addition of GG and the different cosolutes, which is more evident in the case of chaotropic species. The only exception is represented by the fluoride ion, that exhibits a slightly reduced value: the high charge density of F^- leads to the formation of oriented hydrogen bonds in water, resulting in a decrease of the contribution of liquid-like water (Nucci & Vanderkooi, 2008).

Peak 2, which is assigned to the O—H stretching in asymmetric structures and non-linear HBs, shows a significant decrease in the relative peak area upon guar gum and salt addition. The effect is more

Table 1
Peak maximum (cm^{-1}), Center of Gravity (CoG, cm^{-1}) and bandwidth (FWHM, cm^{-1}) for the O—H stretching band, along with the relative areas (%), maximum peak position (cm^{-1}) and peak shift $\Delta\nu$ (cm^{-1}) for the deconvoluted peaks.

	O-H stretching band			Deconvoluted bands								
	Peak maximum (cm^{-1})	CoG (cm^{-1})	FWHM (cm^{-1})	Relative area (%)			Peak maximum (cm^{-1})			$\Delta\underline{\nu}$ (cm^{-1})		
				Peak 1	Peak 2	Peak 3	Peak 1	Peak 2	Peak 3	Peak 1	Peak 2	Peak 3
Pure water	3321	3346	389	4.0	45.7	50.3	3589	3427	3260	0	0	0
GG 1% no salt	3307	3306	440	4.9	12.1	83.0	3584	3455	3273	−5	28	13
Trehalose	3374	3324	432	4.9	18.9	76.2	3574	3452	3290	−15	25	30
Na_2SO_4	3383	3335	427	4.8	20.9	74.4	3583	3458	3297	−6	31	37
NaF	3378	3338	435	3.3	28.8	68.0	3576	3454	3285	−13	27	25
NaCl	3400	3355	413	5.5	25.4	69.1	3591	3464	3304	2	37	44
NaBr	3410	3363	408	6.4	30.0	63.6	3590	3465	3303	1	38	43
NaI	3406	3359	416	5.5	26.0	68.5	3588	3467	3307	−1	40	47
NaSCN	3422	3365	399	6.9	30.7	62.4	3583	3466	3313	−6	39	53
Urea	3398	3352	416	5.4	25.8	68.8	3588	3465	3304	−1	38	44

pronounced in the GG/water dispersion and in the presence of kosmotropic species. An opposite trend is observed for peak 3, which is related to strong intermolecular and symmetrical HBs: for all the samples the relative area is higher if compared to pure water, but moving from kosmotropic to chaotropic species the area values progressively decrease.

From the analysis of the peak shift, the addition of guar gum induces a remarkable shift in peaks 2 and 3 towards higher wavenumbers with respect to pure water. The blue-shift becomes more pronounced according to the increasingly chaotropic nature of the cosolutes. For peak 1, in the presence of kosmotropic species the maximum is shifted to lower wavenumbers, while for chaotropic species no significant variation is detected.

The data reflect the predominant contribution of the polysaccharide in promoting the formation of strongly oriented and symmetrical HBs, which brings about a decrease in the water molecules fraction incorporated into distorted or partially destroyed networks. However, the contribution of the different salts and cosolutes according to the Hofmeister series is not easily interpretable and presents some nonobvious features, like the non-cooperative effect of kosmotropic species in strengthening the structuredness of the HB network.

An alternative approach based on an *unsupervised* chemometric method, PCA, is applied to detect potential specific ion effects within the IR spectral dataset. PCA is commonly adopted to visualize trends and patterns in experimental data, allowing for the identification of groups of samples sharing similar features, like for example the kosmotropic/chaotropic character of a given ionic or neutral cosolute. The main advantage of this method is that it relies exclusively on experimental data and does not require any a priori information about the classification of the samples. Moreover, PCA implementation is rapid and relatively easy, allowing for a reduction of the data complexity, and highlighting the most important features (i.e. wavenumbers) that primarily contribute to sample differentiation based on their lyotropic nature. In this perspective, PCA was performed on the ATR-FTIR dataset by constructing a data matrix in which each sample is represented by its preprocessed spectrum (first derivative followed by normalization), and each variable corresponds to an individual wavenumber. The spectral information is reduced to a small number of orthogonal components that capture the predominant variations induced by the different salts and cosolutes. The score and the loading plot obtained from PCA on the FTIR data are shown in Fig. 2.

The first two principal components (PC1 and PC2) account for 94.1% and 4.9% of the total variance respectively. High variance values explained by a single component can be observed in spectroscopic datasets where one component describes most of the global spectral variability arising from strongly correlated variables, while additional components can account for systematic differences among the samples (Biancolillo et al., 2020; Szymanska-Chargot & Zdunek, 2013). The PC1 vs PC2 score plot shows a good differentiation among the samples according to the kosmotropic/chaotropic nature of the added cosolutes. The samples are distributed along PC1 following the same trends observed for the O—H stretching band intensity, providing an immediate and correct visualization of the anion and cosolutes ranking based on the Hofmeister series. The second principal component (PC2) contributes to samples differentiation, albeit to a lesser extent, and this effect is more evident for chaotropic species. A minor overlap between the two clusters occurs in correspondence of Cl^-, which is usually considered the break point between chaotropic and kosmotropic species (Acar, Tatini, Budroni, et al., 2024). In fact, if one draws two straight lines in the PC coordinate system, one for the kosmotropic and one the chaotropic species, these two intersect exactly where the intermediate chloride is located. This data trend is usually referred to as a "volcano plot": the graph displays a characteristic inverted "*V*" shape, where the data points generally follow a linear increase in a roughly linear and consistent manner up to a peak, and then decrease in a similarly linear fashion, with the downward slope having an absolute value close to that of the upward slope (Mazzini & Craig, 2018). Volcano-shape trends has been extensively reported in the investigation of Hofmeister phenomena, typically emerging when specific physicochemical properties are plotted as a function of ion-specific descriptors (Gregory et al., 2022; Lo Nostro et al., 2010; Lo Nostro & Ninham, 2012). In our case, although the experimental data are represented in a new coordinate system defined by linear combinations of the original variables (i.e. wavenumbers), the characteristic volcano profile remains clearly visible. The two linear trends, for kosmotropes (including trehalose) and for chaotropes (including urea) span across all the investigated salts and also the pristine sample ("no salt"). The only evident deviation is due to sulfate, probably due to its double charge.

The analysis of the loadings indicates that the spectral regions between 3000–3700 cm^{-1} and 1500–1800 cm^{-1} provide the most significant contribution to sample separation along PC1. These wavenumber ranges correspond to the two primary bands in the FTIR spectra, specifically the O—H stretching and O—H bending signals. This finding was expected, since these signals exhibit distinct variations in response to the addition of different cosolutes. The analysis of the loadings on PC2 provides more useful insights about the sample differentiation: besides

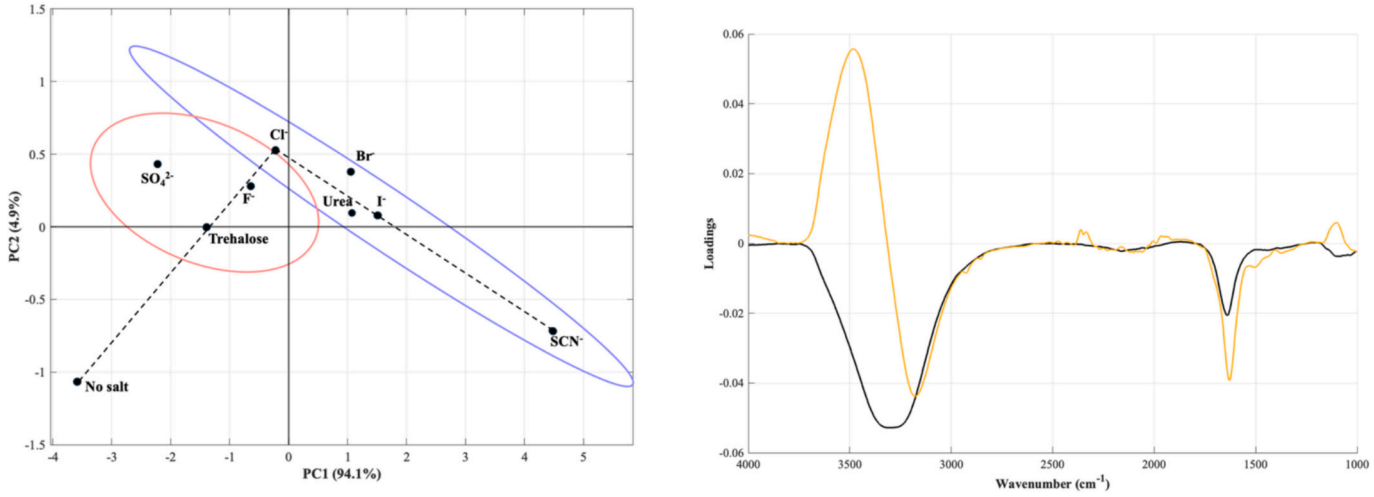


Fig. 2. Left panel: PCA score plot for the FTIR data with 95% confidence ellipsoids estimated for the kosmotropic (red) and chaotropic (blue) species. Right panel: loading plot for PC1 (black) and PC2 (orange). The dotted lines are guidelines for the eye. (For interpretation of the references to colour in this figure legend, the reader is referred to the web version of this article.)

the well-defined contribution between 1500 and 1800 cm^{-1}, two other distinct contributions centered approximately at 3450 and 3200 cm^{-1} show the highest loading values with positive and negative sign, respectively. From the comparison with the results obtained from the deconvolution of the O—H stretching band, these two wavenumber regions show a near-perfect match with peak 2 and peak 3. We recall that peak 2 is associated to distorted, non-linear structures within the hydrogen bond network, while peak 3 is related to strong intermolecular and symmetrical hydrogen bonds. The opposite signs of the loading values indicate that these two contributions have an opposite effect on the sample distribution, which is consistent with the trend observed for the deconvoluted peaks. Upon the addition of GG and the different cosolutes, the relative area of peak 2 decreases, while peak 3 shows a simultaneous increase (see Table 1 and Fig. S7 in the Supplementary Material). The loading analysis confirms also that the influence of peak 1, centered around 3580 cm^{-1}, is negligible.

3.2. Thermogravimetric analysis (TGA)

Thermogravimetric analyses were carried out to evaluate the influence of the different cosolutes on the thermal behavior of the GG dispersions. The TGA and the first derivative of the weight loss (DTG) curves for each sample are shown in Fig. 3, while the stacked thermograms are reported in Fig. S10 and S11 in the Supplementary Material.

For all the samples the predominant weight loss in the TGA curves occurs between 40 and 140 °C due to sample dehydration, while the thermal decomposition of trehalose and urea can be observed in the ranges 250–330 °C and 140–200 °C, respectively. Small but systematic differences in the dehydration behavior can be detected among the investigated systems. In particular, the onset temperatures associated with the initial dehydration processes, calculated from the TGA curves through tangent–baseline intersection and reported in Table S2 in the Supplementary Material, show that the pristine guar gum dispersion exhibits the highest onset temperature. The addition of salts and cosolutes generally shifts the onset of dehydration towards lower

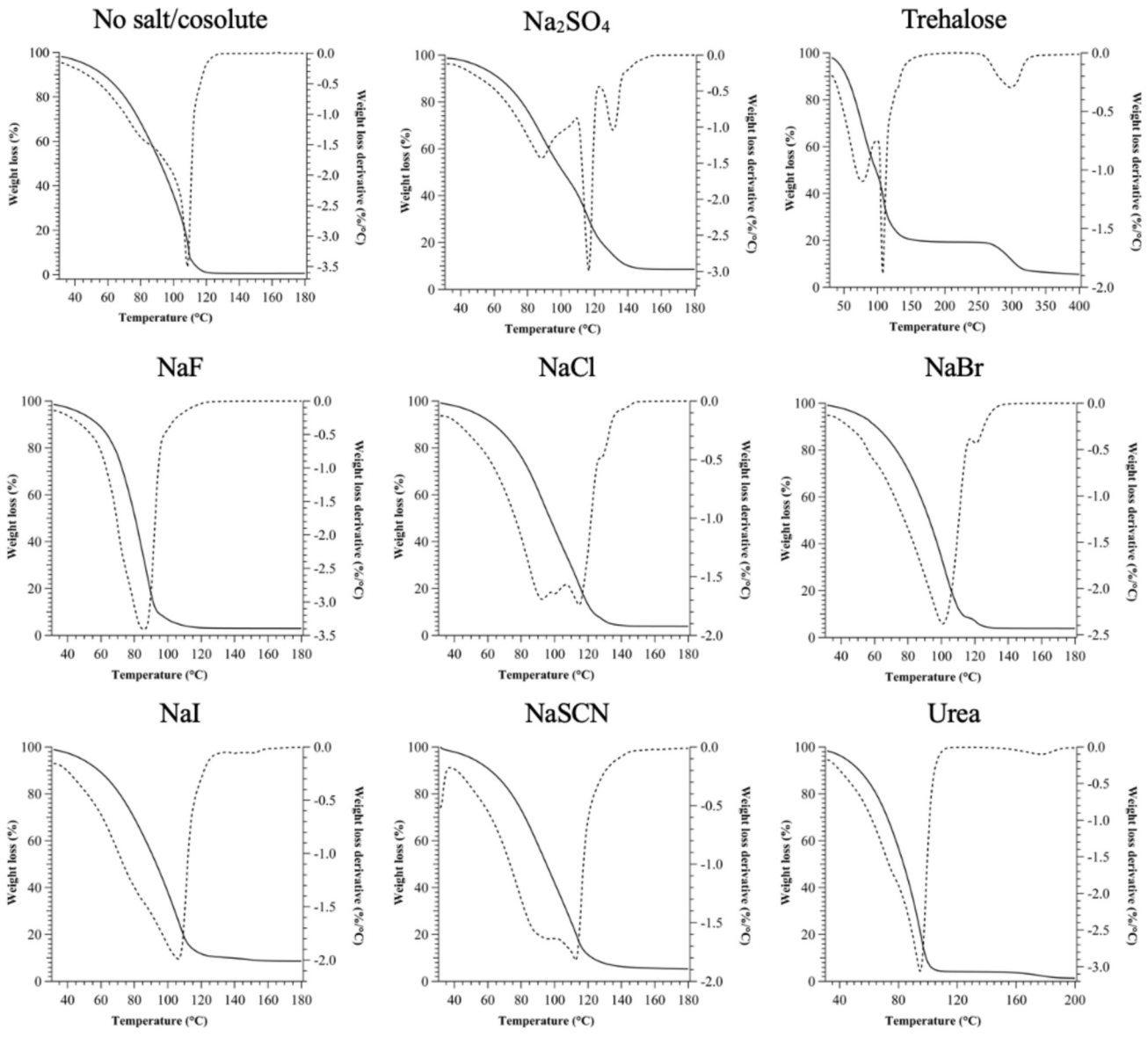


Fig. 3. TGA (solid line) and DTG (dashed line) curves for GG 1% dispersion and GG in the presence of 0.5 M Na_2SO_4, trehalose, NaF, NaCl, NaBr, NaI, NaSCN and urea.

temperatures, suggesting a modification of the original guar gum–water hydration environment. Although some trends can be observed depending on the nature of the added species, the onset temperatures do not follow a defined Hofmeister ordering, likely reflecting the combined contribution of multiple overlapping dehydration processes and different polysaccharide–water interactions. The DTG thermograms show two main contributions in the dehydration signal approximately at 80 °C and 110 °C, corresponding to the evaporation of free and bound water, respectively (Wang et al., 2016). These contributions partially overlap and, in some cases, appear as a single convoluted peak. In the sample containing Na_2SO_4, an additional well-defined peak emerges around 120–130 °C, whereas in most other samples this contribution appears as a shoulder signal. Considering the position and the magnitude, this contribution may be associated to the presence of strongly bound water molecules that evaporate at higher temperatures. Interestingly, a similar behavior was observed in the case of hydrated smectites, where the occurrence of high-temperature shoulder peaks is related to the presence of interlayer cations (Derkowski & Kuligiewicz, 2022). Water molecules form strong hydration shells around sulfate ions, and the energy required for the dehydration process is proportional to the cation's hydration enthalpy. In our systems, we propose a similar mechanism: the hydration of the polysaccharide chains is mediated by the presence of the different anions and the interaction strength depends on the anion's hydration enthalpies, which are listed in Table S3 in the Supplementary Material. As a result, the high-temperature contribution in the dehydration profile is more pronounced for SO_4^{2-}, appears as a shoulder for Cl^- and Br^-, and disappears for I^- and SCN^-. The only exception in the series is represented by F^- that does not show this contribution despite its relatively large negative hydration enthalpy (Marcus, 1987). A similar behavior is observed in the case of non-ionic cosolutes: a shoulder is visible in the DTG thermograms of trehalose at high dehydration temperature, whereas it disappears in the presence of urea.

The analysis of the TGA and DTG curves reveals no additional evidence of distinctive specific ion effects in the thermal profile of GG dispersions. Therefore, an explorative PCA was conducted to identify potential trends within the thermogravimetric data, according to the kosmotropic or chaotropic nature of the cosolutes. The DTG data were selected as input for PCA, since the derivative representation enhances the resolution of overlapping thermal events and emphasizes the differences in dehydration and decomposition rates that are less clearly detectable in the raw TGA profiles. For the DTG dataset a 3-principal component model was calculated, accounting for 90.1% of the total variance. The higher number of principal components retained for the DTG dataset likely reflects the more complex and distributed nature of the thermal events associated with dehydration processes. The 3D score plot and the corresponding loading plot are shown in Fig. 4. The 2D plots are reported in Fig. S12 in the Supplementary Material.

The DTG score plot reveals a good differentiation between kosmotropic and chaotropic species, although a partial overlap between the two clusters occurs. The analysis of the DTG loadings shows that PC1 is characterized by two main contributions of opposite sign, located at approximately 80–90 °C and 100–110 °C, corresponding to the evaporation of free and bound water, respectively. PC2, which provides the most effective discrimination between samples, displays a prominent feature around 110 °C followed by a sharp contribution at 117 °C. These loadings can be attributed to strongly bound water, as evidenced in the DTG profiles (see Fig. 3). However, a more precise assignment of these signals in terms of specific water populations associated to different degrees of interaction with the polymer network should be considered only tentative, and further studies are necessary for a more rigorous interpretation. PC3 exhibits a dual pattern similar to PC1, although the contribution associated to free water appears at slightly higher temperatures.

As in the case of FTIR data, PCA represents a useful tool to visualize sample clustering in DTG datasets according to the Hofmeister series. While direct inspection of individual thermogravimetric profiles can reveal specific ion effects, the analysis of PCA loadings offer a more immediate and integrative perspective, highlighting the key thermal transitions that drive the observed clustering.

3.3. Data fusion

To further improve samples differentiation and gain a deeper understanding of the specific contributions provided by the two individual techniques, the application of data fusion strategy based on the ComDim analysis is explored. As described in the Materials and Methods section, the individual data blocks from ATR-FTIR and thermogravimetric analysis are normalized by their norm and concatenated, then the Common Dimensions (CD) are extracted. For the thermogravimetric data, the first derivative of the weight loss as a function of temperature (DTG) was used as input. A model based on 3 CD is computed from the ComDim analysis, accounting for the 96% of the total variance. The three-dimensional ComDim score plot along with the saliences for each

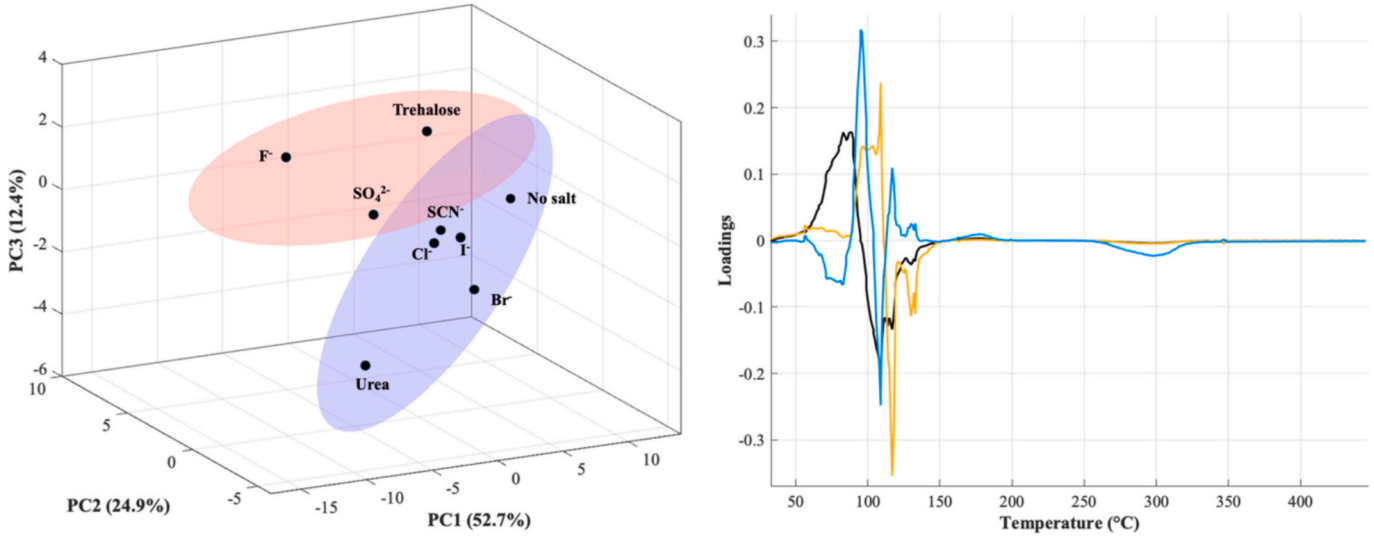


Fig. 4. Left panel: 3D PCA score plot for DTG data with 95% confidence ellipsoids estimated for the kosmotropic (red) and chaotropic (blue) species. Right panel: loading plot for PC1 (black), PC2 (orange) and PC3 (light blue) for DTG. (For interpretation of the references to colour in this figure legend, the reader is referred to the web version of this article.)

common dimension are shown in Fig. 5, while the 2D score plots and the ComDim loadings are reported in Fig. S13 and S14 in the Supplementary Material.

The application of the ComDim data fusion algorithm to the ATR-FTIR and DTG datasets significantly enhances the overall interpretability and sample discrimination capacity if compared to individual techniques. As shown in Fig. 5, the 3D ComDim score plot reveals a distinct clustering based on the kosmotropic/chaotropic nature of the cosolutes without overlapping areas. The intermediate position of Cl^- reflects its borderline behavior between kosmotropic and chaotropic identities, while the pristine GG water dispersion with no added salt is well separated in the common dimensions space, likely due to the absence of ion-induced structuring or interfacial effects. The ComDim salience plot (Fig. 5) highlights the relative contribution of each data block (ATR-FTIR and DTG) to the three CDs. CD1 is predominantly driven by the ATR-FTIR block, indicating that this component reflects the spectroscopic trends related to the different hydration features of the ions. On the other hand, CD2 is mainly influenced by DTG, highlighting a sample differentiation based on thermal transitions along this dimension, while CD3 shows minor yet more balanced contributions from both techniques.

To further elucidate the nature of the extracted dimensions, the loadings for each CD were plotted against the original variables (i.e. wavenumber and temperature) for both data blocks in Fig. S14 in the Supplementary Material. In the ATR-FTIR block, CD1 loadings show two predominant contributions in the OH stretching region centered approximately at 3500 and 3170 cm^{-1}, which are consistent with the modifications in hydrogen bonding networks induced by the addition of cosolutes. CD2 and CD3 loadings show smaller but distinct variations between 1450 and 1700 cm^{-1} (OH bending, esters and amide signals from amino acids impurities) as well in the fingerprint region around 1200–1000 cm^{-1}. In the DTG block, CD2 and CD3 loadings reveal strong signals in the 80–130 °C range, which correspond to water evaporation processes and reflect sample specific dehydration profiles. These findings are consistent with the results obtained from the individual datasets and demonstrate how the ComDim algorithm can effectively identify complementary sources of variation across techniques, enabling a more comprehensive understanding of the Hofmeister effects in polysaccharide-based systems.

4. Conclusions

This study investigated the influence of kosmotropic and chaotropic cosolutes on the hydration and thermal behavior of guar gum aqueous dispersions by integrating ATR-FTIR spectroscopy and thermogravimetric analysis with multivariate and data fusion methods. The results showed that ion-specific effects induce remarkable variations in both the hydrogen-bonding environment and the dehydration behavior of the galactomannan system, confirming the strong coupling between cosolute nature, water structuring, and polysaccharide hydration.

The ATR-FTIR analysis revealed systematic variations in the OH stretching region associated with changes in hydrogen-bonded water populations, while DTG profiles highlighted differences in the thermal stability of hydration water. In both cases, PCA allowed for a rapid unsupervised clustering of the samples in agreement with their position along the Hofmeister series, and identified specific spectral regions and temperature ranges as key discriminative features.

The subsequent application of the ComDim algorithm to the fused ATR-FTIR/DTG dataset further enhanced sample differentiation by identifying shared and complementary features across the experimental techniques. The ComDim score plots showed an improved clustering and a clearer separation between kosmotropic, chaotropic and “borderline” samples, while the analysis of saliences and loadings elucidated the dominant contributions of each data block to the extracted dimensions.

Overall, the combined use of spectroscopic, thermogravimetric, and multiblock chemometric approaches provided an integrated interpretation of ion-dependent perturbations within the guar gum–water network. Beyond the specific case of guar gum dispersions, the proposed strategy may also be extended in future studies to other polysaccharides, alternative solvents and, more in general, to complex macromolecular systems in which solvent-mediated interactions play a critical role.

Glossary

ATR-FTIR	Attenuated Total Reflectance-Fourier Transform Infrared
CCSWA	Common Components and Specific Weights Analysis
CD	Common Dimension
CoG	Center of Gravity
ComDim	Common Dimension Algorithm
DTG	Derivative Thermogravimetry
FWHM	Full Width at Half Maximum

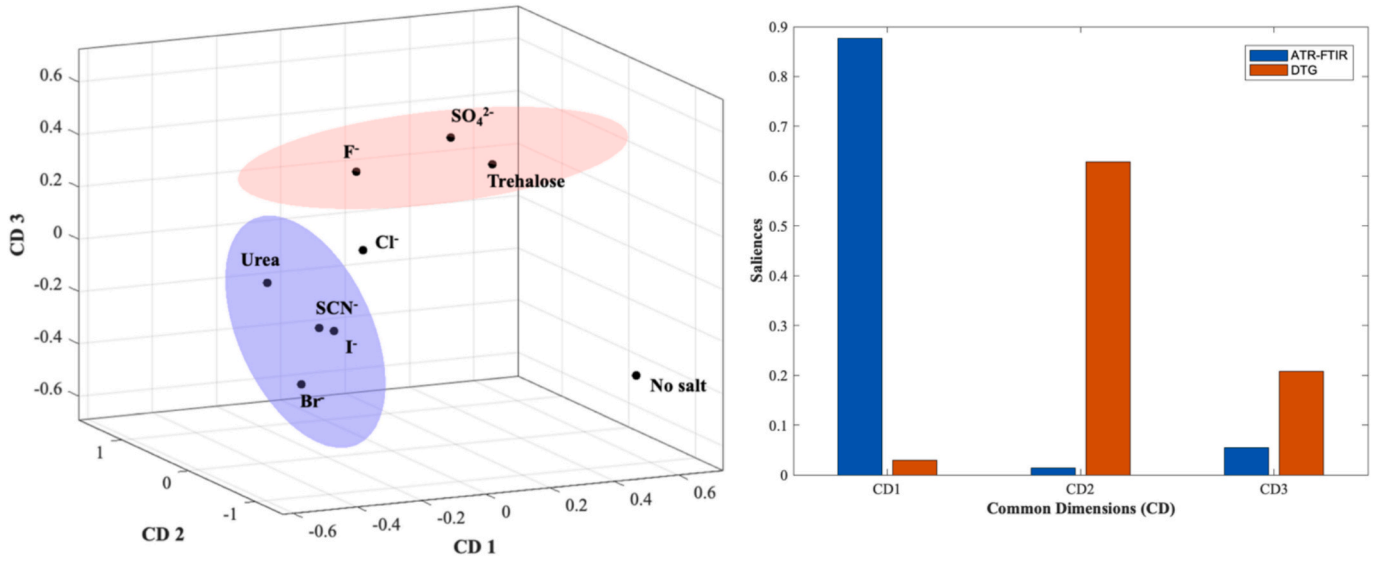


Fig. 5. Left: 3D ComDim score plot for the GG dispersions obtained from the ATR-FTIR and DTG fused dataset, along with the 95% confidence ellipsoids estimated for the kosmotropic (red) and chaotropic (blue) species. Right: ComDim saliences' plot for each common dimension. (For interpretation of the references to colour in this figure legend, the reader is referred to the web version of this article.)

GG	Guar Gum
HB	Hydrogen Bond
PC	Principal Component
PCA	Principal Component Analysis
TGA	Thermogravimetric Analysis

CRediT authorship contribution statement

Duccio Tatini: Writing – review & editing, Writing – original draft, Methodology, Investigation, Formal analysis, Data curation, Conceptualization. **Mert Acar:** Writing – review & editing, Visualization, Validation, Investigation, Data curation. **Michele Baglioni:** Writing – review & editing, Visualization, Methodology. **Gabriella Tamasi:** Writing – review & editing, Visualization, Methodology. **Claudio Rossi:** Writing – review & editing, Supervision, Methodology. **Pierandrea Lo Nostro:** Writing – review & editing, Writing – original draft, Supervision, Resources, Investigation, Conceptualization.

Funding sources

This research did not receive any specific grant from funding agencies in the public, commercial, or not-for-profit sectors.

Declaration of competing interest

The authors declare that they have no known competing financial interests or personal relationships that could have appeared to influence the work reported in this paper.

Acknowledgements

The authors acknowledge partial financial support from the Italian Ministry for the University and Research (MUR, Rome).

Appendix A. Supplementary data

Supplementary data to this article can be found online at https://doi.org/10.1016/j.carbpol.2026.125616.

Data availability

Data will be made available on request.

References

Abidi, N., Cabrales, L., & Haigler, C. H. (2014). Changes in the cell wall and cellulose content of developing cotton fibers investigated by FTIR spectroscopy. *Carbohydrate Polymers, Biopolymers for Life, 100*, 9–16. https://doi.org/10.1016/j.carbpol.2013.01.074

Acar, M., Tatini, D., Budroni, M. A., Ninham, B. W., Rustici, M., Rossi, F., & Lo Nostro, P. (2024). Specific anion effects on urease activity: A Hofmeister study. *Colloids and Surfaces B: Biointerfaces, 236*, Article 113789. https://doi.org/10.1016/j.colsurfb.2024.113789

Acar, M., Tatini, D., Fidi, A., Pacini, L., Quagliata, M., Nuti, F., … Lo Nostro, P. (2024). A promising compound for green multiresponsive materials based on acyl carrier protein. *Langmuir, 40*(24), 12381–12393. https://doi.org/10.1021/acs.langmuir.4c00476

Acar, M., Tatini, D., Ninham, B. W., & Lo Nostro, P. (2025). The role of polarizability in isoelectronic ions: The case of pseudohalides. *Molecules, 30*(2), Article 2. https://doi.org/10.3390/molecules30020323

Anjum, A., Zuber, M., Zia, K. M., Anjum, M. N., & Aftab, W. (2021). Preparation and characterization of guar gum based polyurethanes. *International Journal of Biological Macromolecules, 183*, 2174–2183. https://doi.org/10.1016/j.ijbiomac.2021.06.025

Azcarate, S. M., Ríos-Reina, R., Amigo, J. M., & Goicoechea, H. C. (2021). Data handling in data fusion: Methodologies and applications. *TrAC Trends in Analytical Chemistry, 143*, Article 116355. https://doi.org/10.1016/j.trac.2021.116355

Barbar, R., Mayer-Laigle, C., Beaugrand, J., Cuq, B., & Barron, C. (2023). Comparison of hydration water properties of common and durum wheat brans upon grinding with different loading modes. *Journal of Cereal Science, 114*, Article 103786. https://doi.org/10.1016/j.jcs.2023.103786

Beattie, J. R., & Esmonde-White, F. W. L. (2021). Exploration of principal component analysis: Deriving principal component analysis visually using spectra. *Applied Spectroscopy, 75*(4), 361–375. https://doi.org/10.1177/0003702820987847

Biancolillo, A., Boqué, R., Cocchi, M., & Marini, F. (2019). Data fusion strategies in food analysis. In *, 31. Data handling in science and technology* (pp. 271–310). Elsevier. https://doi.org/10.1016/B978-0-444-63984-4.00010-7.

Biancolillo, A., Marini, F., Ruckebusch, C., Vitale, R., Biancolillo, A., Marini, F., … Vitale, R. (2020). Chemometric strategies for spectroscopy-based food authentication. *Applied Sciences, 10*(18). https://doi.org/10.3390/app10186544

Binder, H. (2007). Water near lipid membranes as seen by infrared spectroscopy. *European Biophysics Journal, 36*(4), 265–279. https://doi.org/10.1007/s00249-006-0110-6

Borghini, F., Tamasi, G., Loiselle, S. A., Baglioni, M., Ferrari, S., Bisozzi, F., … Rossi, C. (2024). Phenolic profiles in olive leaves from different cultivars in Tuscany and their use as a marker of varietal and geographical origin on a small scale. *Molecules, 29*(15), Article 3617. https://doi.org/10.3390/molecules29153617

Borràs, E., Ferré, J., Boqué, R., Mestres, M., Aceña, L., & Busto, O. (2015). Data fusion methodologies for food and beverage authentication and quality assessment – A review. *Analytica Chimica Acta, 891*, 1–14. https://doi.org/10.1016/j.aca.2015.04.042

Boström, M., Williams, D. R. M., Stewart, P. R., & Ninham, B. W. (2003). Hofmeister effects in membrane biology: The role of ionic dispersion potentials. *Physical Review E, 68*(4), Article 041902. https://doi.org/10.1103/PhysRevE.68.041902

Bro, R., & Smilde, A. K. (2014). Principal component analysis. *Analytical Methods, 6*(9), 2812–2831. https://doi.org/10.1039/C3AY41907J

Cacace, M. G., Landau, E. M., & Ramsden, J. J. (1997). The Hofmeister series: Salt and solvent effects on interfacial phenomena. *Quarterly Reviews of Biophysics, 30*(3), 241–277. https://doi.org/10.1017/s0033583597003363

Cariou, V., Qannari, E. M., Rutledge, D. N., & Vigneau, E. (2018). ComDim: From multiblock data analysis to path modeling. *Food Quality and Preference, Sensometrics 2016: Sensometrics-By-The-Sea, 67*, 27–34. https://doi.org/10.1016/j.foodqual.2017.02.012

Cheng, Y., Brown, K. M., & Prud'homme, R. K. (2002). Preparation and characterization of molecular weight fractions of guar galactomannans using acid and enzymatic hydrolysis. *International Journal of Biological Macromolecules, 31*(1), 29–35. https://doi.org/10.1016/S0141-8130(02)00046-6

Cordella, C. B. Y. (2012). PCA: The basic building block of chemometrics. In *Analytical chemistry*. IntechOpen. https://doi.org/10.5772/51429.

Cunha, P. L. R., Paula, R. C. M.d., & Feitosa, J. P. A. (2007). Purification of guar gum for biological applications. *International Journal of Biological Macromolecules, 41*(3), 324–331. https://doi.org/10.1016/j.ijbiomac.2007.04.003

Derkowski, A., & Kuligiewicz, A. (2022). Thermal analysis and thermal reactions of smectites: A review of methodology, mechanisms, and kinetics. *Clays and Clay Minerals, 70*(6), 946–972. https://doi.org/10.1007/s42860-023-00222-y

Enev, V., Sedláček, P., Jarábková, S., Velcer, T., & Pekař, M. (2019). ATR-FTIR spectroscopy and thermogravimetry characterization of water in polyelectrolyte-surfactant hydrogels. *Colloids and Surfaces A: Physicochemical and Engineering Aspects, 575*, 1–9. https://doi.org/10.1016/j.colsurfa.2019.04.089

García, Y. F., Solís, M. F. M.d. C., Gómez-Angulo, J. H., Preciado, A. H. M., Silva-Jara, J. M., Rosa, J. D. P.d.l., & Escalante-Garcia, Z. Y. (2025). Industrial applications, principal sources, and extraction of galactomannans: A review. *Foods, 14*(9). https://doi.org/10.3390/foods14091587

George, A., Shah, P. A., & Shrivastav, P. S. (2019). Guar gum: Versatile natural polymer for drug delivery applications. *European Polymer Journal, 112*, 722–735. https://doi.org/10.1016/j.eurpolymj.2018.10.042

Greenacre, M., Groenen, P. J. F., Hastie, T., D'Enza, A. I., Markos, A., & Tuzhilina, E. (2022). Principal component analysis. *Nature Reviews Methods Primers, 2*(1), 1–21. https://doi.org/10.1038/s43586-022-00184-w

Gregory, K. P., Elliott, G. R., Robertson, H., Kumar, A., Wanless, E. J., Webber, G. B., … Page, A. J. (2022). Understanding specific ion effects and the Hofmeister series. *Physical Chemistry Chemical Physics, 24*(21), 12682–12718. https://doi.org/10.1039/D2CP00847E

Grossutti, M., & Dutcher, J. R. (2016). Correlation between chain architecture and hydration water structure in polysaccharides. *Biomacromolecules, 17*(3), 1198–1204. https://doi.org/10.1021/acs.biomac.6b00026

Grossutti, M., & Dutcher, J. R. (2020). Hydration water structure, hydration forces, and mechanical properties of polysaccharide films. *Biomacromolecules, 21*(12), 4871–4877. https://doi.org/10.1021/acs.biomac.0c01098

Houhou, R., & Bocklitz, T. (2021). Trends in artificial intelligence, machine learning, and chemometrics applied to chemical data. *Analytical Science Advances, 2*(3–4), 128–141. https://doi.org/10.1002/ansa.202000162

Jakubowska, A., & Kozik, T. (2019). Chemometric study of kosmotropic and chaotropic ion properties related to Hofmeister effects. *Journal of Chemometrics, 33*(11), Article e3187. https://doi.org/10.1002/cem.3187

Jenkins, H. D. B., & Marcus, Y. (1995). Viscosity B-coefficients of ions in solution. *Chemical Reviews, 95*(8), 2695–2724. https://doi.org/10.1021/cr00040a004

Jiang, Q., Yan, X., & Zhao, W. (2013). Fault detection and diagnosis in chemical processes using sensitive principal component analysis. *Industrial & Engineering Chemistry Research, 52*(4), 1635–1644. https://doi.org/10.1021/ie3017016

Jolliffe, I. T., & Cadima, J. (2016). Principal component analysis: A review and recent developments. *Philosophical Transactions of the Royal Society A: Mathematical, Physical and Engineering Sciences, 374*(2065), Article 20150202. https://doi.org/10.1098/rsta.2015.0202

Jouan-Rimbaud Bouveresse, D., Pinto, R. C., Schmidtke, L. M., Locquet, N., & Rutledge, D. N. (2011). Identification of significant factors by an extension of

ANOVA–PCA based on multi-block analysis. *Chemometrics and Intelligent Laboratory Systems, 106*(2), 173–182. https://doi.org/10.1016/j.chemolab.2010.05.005
Kemsley, E. K., Defernez, M., & Marini, F. (2019). Multivariate statistics: Considerations and confidences in food authenticity problems. *Food Control, 105*, 102–112. https://doi.org/10.1016/j.foodcont.2019.05.021
Kitadai, N., Sawai, T., Tonoue, R., Nakashima, S., Katsura, M., & Fukushi, K. (2014). Effects of ions on the OH stretching band of water as revealed by ATR-IR spectroscopy. *Journal of Solution Chemistry, 43*(6), 1055–1077. https://doi.org/10.1007/s10953-014-0193-0
Kunz, W., Henle, J., & Ninham, B. W. (2004). Zur Lehre von der Wirkung der Salze' (about the science of the effect of salts): Franz Hofmeister's historical papers. *Current Opinion in Colloid & Interface Science, 9*(1), 19–37. https://doi.org/10.1016/j.cocis.2004.05.005
Li Vigni, M., Durante, C., & Cocchi, M. (2013). Chapter 3—Exploratory data analysis. In F. Marini (Ed.), *28. Data handling in science and technology* (pp. 55–126). Elsevier. https://doi.org/10.1016/B978-0-444-59528-7.00003-X.
Lin, J., Huang, Y., & Wang, S. (2020). The Hofmeister effect on protein hydrogels with stranded and particulate microstructures. *Colloids and Surfaces B: Biointerfaces, 196*, Article 111332. https://doi.org/10.1016/j.colsurfb.2020.111332
Liu, D., Ma, G., Levering, L. M., & Allen, H. C. (2004). Vibrational spectroscopy of aqueous sodium halide solutions and air−liquid interfaces: Observation of increased interfacial depth. *The Journal of Physical Chemistry B, 108*(7), 2252–2260. https://doi.org/10.1021/jp036169r
Liyanage, S., Abidi, N., Auld, D., & Moussa, H. (2015). Chemical and physical characterization of galactomannan extracted from guar cultivars (*Cyamopsis tetragonolobus* L.). *Industrial Crops and Products, 74*, 388–396. https://doi.org/10.1016/j.indcrop.2015.05.013
Lo Nostro, P., & Ninham, B. W. (2012). Hofmeister phenomena: An update on ion specificity in biology. *Chemical Reviews, 112*(4), 2286–2322. https://doi.org/10.1021/cr200271j
Lo Nostro, P., Peruzzi, N., Severi, M., Ninham, B. W., & Baglioni, P. (2010). Asymmetric partitioning of anions in lysozyme dispersions. *Journal of the American Chemical Society, 132*(18), 6571–6577. https://doi.org/10.1021/ja101603n
Madeira, P. P., Titus, A. R., Ferreira, L. A., Belgovskiy, A. I., Mann, E. K., Jay Adin Mann, J., … Zaslavsky, B. Y. (2021). Hydrogen bond arrangement is shown to differ in coexisting phases of aqueous two-phase systems. *Biomolecules, 11*(12). https://doi.org/10.3390/biom11121787
Marcus, Y. (1987). The thermodynamics of solvation of ions. Part 2.—The enthalpy of hydration at 298.15 K. *Journal of the Chemical Society, Faraday Transactions 1: Physical Chemistry in Condensed Phases, 83*(2), 339–349. https://doi.org/10.1039/F19878300339
Marcus, Y. (1991). Thermodynamics of solvation of ions. Part 5.—Gibbs free energy of hydration at 298.15 K. *Journal of the Chemical Society, Faraday Transactions, 87*(18), 2995–2999. https://doi.org/10.1039/FT9918702995
Marinov, V. S., Nickolov, Z. S., & Matsuura, H. (2001). Raman spectroscopic study of water structure in aqueous nonionic surfactant solutions. *The Journal of Physical Chemistry B, 105*(41), 9953–9959. https://doi.org/10.1021/jp011936c
Mazzini, V., & Craig, V. S. J. (2018). Volcano plots emerge from a sea of nonaqueous solvents: The law of matching water affinities extends to all solvents. *ACS Central Science, 4*(8), 1056–1064. https://doi.org/10.1021/acscentsci.8b00348
McKenzie, J. S., Donarski, J. A., Wilson, J. C., & Charlton, A. J. (2011). Analysis of complex mixtures using high-resolution nuclear magnetic resonance spectroscopy and chemometrics. *Progress in Nuclear Magnetic Resonance Spectroscopy, 59*(4), 336–359. https://doi.org/10.1016/j.pnmrs.2011.04.003
Mishra, P., Roger, J.-M., Jouan-Rimbaud-Bouveresse, D., Biancolillo, A., Marini, F., Nordon, A., & Rutledge, D. N. (2021). Recent trends in multi-block data analysis in chemometrics for multi-source data integration. *TrAC Trends in Analytical Chemistry, 137*, Article 116206. https://doi.org/10.1016/j.trac.2021.116206
Mishra, P., Roger, J. M., Rutledge, D. N., Biancolillo, A., Marini, F., Nordon, A., & Jouan-Rimbaud-Bouveresse, D. (2020). MBA-GUI: A chemometric graphical user interface for multi-block data visualisation, regression, classification, variable selection and automated pre-processing. *Chemometrics and Intelligent Laboratory Systems, 205*, Article 104139. https://doi.org/10.1016/j.chemolab.2020.104139
Mudgil, D., Barak, S., & Khatkar, B. S. (2012). X-ray diffraction, IR spectroscopy and thermal characterization of partially hydrolyzed guar gum. *International Journal of Biological Macromolecules, 50*(4), 1035–1039. https://doi.org/10.1016/j.ijbiomac.2012.02.031
Musilová, L., Kašpárková, V., Mráček, A., Minařík, A., & Minařík, M. (2019). The behaviour of hyaluronan solutions in the presence of Hofmeister ions: A light scattering, viscometry and surface tension study. *Carbohydrate Polymers, 212*, 395–402. https://doi.org/10.1016/j.carbpol.2019.02.032
Nardin, R., Tamasi, G., Baglioni, M., Bisozzi, F., Consumi, M., Costa, J., … Rossi, C. (2024). Determination of elemental content in vineyard soil, leaves, and grapes of Sangiovese grapes from the chianti region using ICP-MS for geographical identification. *ACS Food Science & Technology, 4*(11), 2585–2599. https://doi.org/10.1021/acsfoodscitech.4c00231
Ninham, B. W., & Yaminsky, V. (1997). Ion binding and ion specificity: The Hofmeister effect and Onsager and Lifshitz theories. *Langmuir, 13*(7), 2097–2108. https://doi.org/10.1021/la960974y
Nucci, N. V., & Vanderkooi, J. M. (2008). Effects of salts of the Hofmeister series on the hydrogen bond network of water. *Journal of Molecular Liquids, 143*(2), 160–170. https://doi.org/10.1016/j.molliq.2008.07.010
Özen, İ., Bahtiyari, M.İ., Haji, A., Islam, S.u., & Wang, X. (2023). Properties of galactomannans and their textile-related applications—A concise review. *International Journal of Biological Macromolecules, 227*, 1001–1014. https://doi.org/10.1016/j.ijbiomac.2022.11.276
Parsons, D. F., Boström, M., Nostro, P. L., & Ninham, B. W. (2011). Hofmeister effects: Interplay of hydration, nonelectrostatic potentials, and ion size. *Physical Chemistry Chemical Physics, 13*(27), 12352–12367. https://doi.org/10.1039/C1CP20538B
Qannari, E. M., Wakeling, I., & MacFie, H. J. H. (1995). A hierarchy of models for analysing sensory data. *Food Quality and Preference, Second Sensometrics Meeting, 6*(4), 309–314. https://doi.org/10.1016/0950-3293(95)00033-X
Rébufa, C., Girard, F., Artaud, J., Dupuy, N., Rébufa, C., Girard, F., … Dupuy, N. (2019). Discrimination by infrared spectroscopy: Application to micronized locust bean and guar gums. In *Modern spectroscopic techniques and applications*. IntechOpen. https://doi.org/10.5772/intechopen.87568.
Robinson, G., Ross-Murphy, S. B., & Morris, E. R. (1982). Viscosity-molecular weight relationships, intrinsic chain flexibility, and dynamic solution properties of guar galactomannan. *Carbohydrate Research, 107*(1), 17–32. https://doi.org/10.1016/S0008-6215(00)80772-7
Rocha Baqueta, M., Coqueiro, A., Henrique Março, P., Mandrone, M., Poli, F., & Valderrama, P. (2021). Integrated 1H NMR fingerprint with NIR spectroscopy, sensory properties, and quality parameters in a multi-block data analysis using ComDim to evaluate coffee blends. *Food Chemistry, 355*, Article 129618. https://doi.org/10.1016/j.foodchem.2021.129618
Rosa, L. N., De Figueiredo, L. C., Bonafé, E. G., Coqueiro, A., Visentainer, J. V., Março, P. H., … Valderrama, P. (2017). Multi-block data analysis using ComDim for the evaluation of complex samples: Characterization of edible oils. *Analytica Chimica Acta, 961*, 42–48. https://doi.org/10.1016/j.aca.2017.01.019
Salis, A., & Ninham, B. W. (2014). Models and mechanisms of Hofmeister effects in electrolyte solutions, and colloid and protein systems revisited. *Chemical Society Reviews, 43*(21), 7358–7377. https://doi.org/10.1039/C4CS00144C
Salvatore, E., Cocchi, M., Marchetti, A., Marini, F., & de Juan, A. (2013). Determination of phenolic compounds and authentication of PDO Lambrusco wines by HPLC-DAD and chemometric techniques. *Analytica Chimica Acta, 761*, 34–45. https://doi.org/10.1016/j.aca.2012.11.015
Sarri, F., Tatini, D., Raudino, M., Ambrosi, M., Carretti, E., & Lo Nostro, P. (2019). Electro-responsive green gels for lower environmental impact shale gas extraction. *Energy & Fuels, 33*(3), 2057–2066. https://doi.org/10.1021/acs.energyfuels.8b04321
Sarri, F., Tatini, D., Tanini, D., Simonelli, M., Ambrosi, M., Ninham, B. W., … Lo Nostro, P. (2018). Specific ion effects in non-aqueous solvents: The case of glycerol carbonate. *Journal of Molecular Liquids, 266*, 711–717. https://doi.org/10.1016/j.molliq.2018.06.120
Sharahi, M., Bahrami, S. H., & Karimi, A. (2025). A comprehensive review on guar gum and its modified biopolymers: Their potential applications in tissue engineering. *Carbohydrate Polymers, 347*, Article 122739. https://doi.org/10.1016/j.carbpol.2024.122739
Sharma, G., Sharma, S., Kumar, A., Al-Muhtaseb, A. H., Naushad, M., Ghfar, A. A., … Stadler, F. J. (2018). Guar gum and its composites as potential materials for diverse applications: A review. *Carbohydrate Polymers, 199*, 534–545. https://doi.org/10.1016/j.carbpol.2018.07.053
Szymanska-Chargot, M., & Zdunek, A. (2013). Use of FT-IR spectra and PCA to the bulk characterization of cell wall residues of fruits and vegetables along a fraction process. *Food Biophysics, 8*(1), 29–42. https://doi.org/10.1007/s11483-012-9279-7
Tamasi, G., Baratto, M. C., Bonechi, C., Byelyakova, A., Pardini, A., Donati, A., … Rossi, C. (2019). Chemical characterization and antioxidant properties of products and by-products from Olea europaea L. *Food Science & Nutrition, 7*(9), 2907–2920. https://doi.org/10.1002/fsn3.1142
Tatini, D., Bisozzi, F., Costantini, S., Fattori, G., Boldrini, A., Baglioni, M., … Rossi, C. (2025). Geographical origin authentication of leaves and drupes from *Olea europaea* via ^{1}H NMR and excitation–emission fluorescence spectroscopy: A data fusion approach. *Molecules, 30*(15), Article 15. https://doi.org/10.3390/molecules30153208
Tatini, D., Ciardi, D., Sofroniou, C., Ninham, B. W., & Lo Nostro, P. (2022). Physicochemical characterization of green sodium oleate-based formulations. Part 2. Effect of anions. *Journal of Colloid and Interface Science, 617*, 399–408. https://doi.org/10.1016/j.jcis.2022.01.135
Tatini, D., Sarri, F., Maltoni, P., Ambrosi, M., Carretti, E., Ninham, B. W., & Lo Nostro, P. (2017). Specific ion effects in polysaccharide dispersions. *Carbohydrate Polymers, 173*, 344–352. https://doi.org/10.1016/j.carbpol.2017.05.078
Tchandao Mangamana, E., Cariou, V., Vigneau, E., Glèlè Kakaï, R. L., & Qannari, E. M. (2019). Unsupervised multiblock data analysis: A unified approach and extensions. *Chemometrics and Intelligent Laboratory Systems, 194*, Article 103856. https://doi.org/10.1016/j.chemolab.2019.103856
Tomassetti, M., Marini, F., Di Natale, C., Castrucci, M., & Campanella, L. (2025). Yeast-based direct catalytic ethanol fuel cell biosensors: A batch analysis apparatus combined with chemometrics for qualitative carbohydrate detection. *Biosensors, 15*(2), Article 2. https://doi.org/10.3390/bios15020096
Tomassetti, M., Marini, F., Pezzilli, R., Castrucci, M., Di Natale, C., & Campanella, L. (2024). Improvement of qualitative analyses of aliphatic alcohols using direct catalytic fuel cell and chemometric analysis format. *Sensors, 24*(10), Article 10. https://doi.org/10.3390/s24103209
Tomassetti, M., Marini, F., Pezzilli, R., Castrucci, M., Di Natale, C., & Campanella, L. (2025). Further improvements on the possibility of carrying out alcohols' qualitative analyses using fuel cells, of the DCMFC type, coupled to chemometric analysis. In S. Conoci, C. Di Natale, L. Prodi, & G. Valenti (Eds.), *Sensors and microsystems* (pp. 140–146). Springer Nature Switzerland. https://doi.org/10.1007/978-3-031-82076-2_20.
Torres, M. D., Hallmark, B., & Wilson, D. I. (2014). Effect of concentration on shear and extensional rheology of guar gum solutions. *Food Hydrocolloids, 40*, 85–95. https://doi.org/10.1016/j.foodhyd.2014.02.011

Voet, A. (1937). Quantative lyotropy. *Chemical Reviews, 20*(2), 169–179. https://doi.org/10.1021/cr60066a001

Vulpitta, V., Corrente, G. A., Gaudio, D., Lano, A., & Beneduci, A. (2025). Integrated physicochemical and chemometric analysis for the detection of Tara gum adulteration. *LWT, 228*, Article 118126. https://doi.org/10.1016/j.lwt.2025.118126

Wang, H., Liu, Y., Li, J., & Luo, J. (2016). Investigation of superlubricity achieved by polyalkylene glycol aqueous solutions. *Advanced Materials Interfaces, 3*(19), Article 1600531. https://doi.org/10.1002/admi.201600531

Wang, H.-P., Chen, P., Dai, J.-W., Liu, D., Li, J.-Y., Xu, Y.-P., & Chu, X.-L. (2022). Recent advances of chemometric calibration methods in modern spectroscopy: Algorithms, strategy, and related issues. *TrAC Trends in Analytical Chemistry, 153*, Article 116648. https://doi.org/10.1016/j.trac.2022.116648

Wang, Q., Ellis, P. R., & Ross-Murphy, S. B. (2003). Dissolution kinetics of guar gum powders—II. Effects of concentration and molecular weight. *Carbohydrate Polymers, 53*(1), 75–83. https://doi.org/10.1016/S0144-8617(03)00009-2

You, Q., Wang, Z., Tian, X., & Xu, X. (2023). A multi-block data approach to assessing beef quality: ComDim analysis of hyperspectral imaging, 1H NMR, electronic nose and quality parameters data. *Food Chemistry, 425*, Article 136469. https://doi.org/10.1016/j.foodchem.2023.136469

Zeaiter, M., & Rutledge, D. (2009). 3.04—Preprocessing methods. In S. D. Brown, R. Tauler, & B. Walczak (Eds.), *Comprehensive chemometrics* (pp. 121–231). Elsevier. https://doi.org/10.1016/B978-044452701-1.00074-0.